Check for updates

The electronic structure and the nature of the chemical bond in CeO$_2$

Konstantin I. Maslakov, [ID] [a] Yury A. Teterin, [ab] Mikhail V. Ryzhkov, [ID] [c] Aleksej J. Popel, [ID] *[d] Anton Yu. Teterin, [b] Kirill E. Ivanov, [b] Stepan N. Kalmykov, [ab] Vladimir G. Petrov, [a] Peter K. Petrov [e] and Ian Farnan [d]

The X-ray photoelectron spectral structure of CeO$_2$ valence electrons in the binding energy range of 0 to ~50 eV was analyzed. The core-electron spectral structure parameters and the results of relativistic discrete-variational calculations of CeO$_8$ and Ce$_{63}$O$_{216}$ clusters were taken into account. Comparison of the valence and the core-electron spectral structures showed that the formation of the inner (IVMO) and the outer (OVMO) valence molecular orbitals contributes to the spectral structure more than the many-body processes. The Ce 4f electrons were established to participate directly in chemical bond formation in CeO$_2$ losing partially their f character. They were found to be localized mostly within the outer valence band. The Ce 5p atomic orbitals were shown to participate in the formation of both the inner and the outer valence molecular orbitals (MOs). A large part in the IVMO formation is taken by the filled Ce 5p$_{1/2}$, 5p$_{3/2}$ and O 2s atomic shells, while the Ce 5s electrons participate weakly in the chemical bond formation. The composition and the sequent order of the molecular orbitals in the binding energy range of 0 to ~50 eV were established. A quantitative scheme for the molecular orbitals of CeO$_2$ was built. This scheme is fundamental for understanding the nature of chemical bonding and also for the interpretation of other X-ray spectra of CeO$_2$. Evaluations revealed that the IVMO electrons weaken the chemical bond formed by the OVMO electrons by 37%.

[a] *Chemistry Department, Lomonosov Moscow State University, Moscow, 119991, Russia*
[b] *NRC "Kurchatov Institute", Moscow, 123182, Russia*
[c] *Institute of Solid State Chemistry, Ural Department of RAS, Ekaterinburg, Russia*
[d] *Department of Earth Sciences, University of Cambridge, Downing Street, Cambridge, CB2 3EQ, UK. E-mail: apopel@cantab.net; Tel: +44 (0)1223 768357*
[e] *Department of Materials and London Centre for Nanotechnology, Imperial College London, London, SW7 2AZ, UK*

1 Introduction

Cerium dioxide is known as a non-radioactive structural substitute of actinide oxides (UO$_2$ and PuO$_2$).[1,2] CeO$_2$-based ceramics are suggested as an inert ^{239}Pu or ^{235}U bearing matrix for nuclear fuel, as well as a matrix for high-level waste disposal.[1,3] CeO$_2$ is also used an exhaust gas afterburning catalyst[4,5] and in electronics.[6]

X-ray photoelectron spectroscopy (XPS) has been widely used for the study of the electronic structure of CeO$_2$.[7–11] The core and valence XPS spectra of cerium compounds are complicated and structured. This complicates the determination of the oxidation state of cerium on the basis of chemical shifts.[7–11] Several mechanisms for the formation of the complex CeO$_2$ XPS structure were considered.

Thus, the authors of ref. 12–16 associated the complex CeO$_2$ XPS structure with the presence of Ce^{3+} and Ce^{4+} ions in the samples (mixed valence). However, the authors of ref. 17 suggested that CeO$_2$ contains only Ce^{4+} ions and on the basis of the calculations they associated the complex Ce 3d XPS structure with the complex final state consisting of the ground final state Ce 3d^{9}4f^0 and the two excited final states 3d^{9}4f^{1}OVMO^{-1} and 3d^{9}5p^{5}np^1. The unusual final state Ce 3d^{9}5p^{5}np^1 was attributed to a weakly screened vacancy in the IVMO.[9,18] These results agree with the experimental core-electron XPS data in ref. 19, which showed that the complex XPS structure appears in the core-electron XPS spectra and does not appear in the valence XPS spectra.

The authors of ref. 18 performed the non-relativistic discrete-variational calculations for the CeO$_8$ cluster including a cerium atom and its nearest environment in CeO$_2$ in the MO binding energy (BE) range of 0–22 eV and qualitatively compared the calculated and experimental spectra. In the present work the valence and the core-level XPS spectra of the single-crystalline CeO$_2$ film on Si(001) were measured, and the relativistic discrete-variational calculations for the CeO$_8$ and Ce$_{63}$O$_{216}$ clusters in the BE range of 0 to ~50 eV were carried out. A quantitative comparison of the calculated and experimental results was performed. A quantitative scheme of the molecular orbitals for CeO$_2$ was built.

This journal is © the Owner Societies 2018

Phys. Chem. Chem. Phys., 2018, **20**, 16167–16175 | 16167

2 Experimental

2.1 Sample production

The CeO$_2$ thin film was grown by pulsed laser deposition on a (001) oriented p-doped Si substrate and characterised by XRD and SEM as described in detail in ref. 20. The thin film of CeO$_2$ has nominal thickness (250 nm). X-ray diffraction analysis suggested that the CeO$_2$ film can be described as a single crystal in a (111) crystallographic orientation.

2.2 X-ray photoelectron measurements

The XPS spectra of CeO$_2$ were recorded on a Kratos Axis Ultra DLD spectrometer using monochromatic Al-Kα radiation ($h\nu$ = 1486.7 eV) at a 150 W X-ray gun power under 1.3×10^{-7} Pa at room temperature. The analyzed area was an ellipse with minor and major axes of 300 and 700 nm, respectively.

A Kratos charge neutraliser system was used and BEs were measured relatively to the BE of the C 1s electrons from hydrocarbons adsorbed on the sample surface, which was found to be equal to 285.0 eV. FWHMs are given relatively to that of the C 1s XPS peak for hydrocarbons on the sample surface to be 1.3 eV.[21] The error in the determination of the BE and the peak width did not exceed ±0.05 eV, and the error of the relative peak intensity was ±5%. The inelastically scattered electron-related background was subtracted by the method of Shirley.[22]

Quantitative elemental and ionic analysis was performed for the surface of the studied sample AP1 on the basis of the valence and core-level XPS spectra. The stoichiometric (CeO$_{1.99}$) and ionic (97% Ce^{4+} and 3% Ce^{3+}) compositions of the studied sample were found. More details on the spectral measurements and elemental and ionic analyses are given in ref. 11.

2.3 Calculations

The calculations of the electronic structure of CeO$_2$ (R_{Ce-O} = 0.2344 nm)[23] were performed for the two types of finite fragments of the crystal lattice: 279-atom Ce$_{63}$O$_{216}$ and small CeO$_8$ clusters. The latter object modeled a cerium atom nearest environment in a dioxide crystal. For the modeling of the boundary conditions for the Ce$_{63}$O$_{216}$ fragment, we used an "extended cluster" scheme described in detail in ref. 24. In this model, the crystal fragment under study consists of two parts: the internal main part (or the "core") and the outer part (or the "shell" of the cluster), the latter part usually includes the atoms of 1–5 coordination spheres surrounding the "core". During the self-consistency procedure, the electron densities and the potential of atoms in the "shell" are replaced by the corresponding values obtained for the crystallographically equivalent centers of the cluster core. In addition to the introduction of the long-range component of the surrounding crystal potential, the extended cluster is embedded in a pseudopotential of the outer crystal lattice, including several thousand centers with Coulomb and exchange–correlation potentials obtained for the corresponding equivalent atoms in the internal part of the cluster. This pseudopotential modeling of the long-range crystal potential becomes important in the calculations of

compounds with noticeable charges on atoms, such as oxides and fluorides.

In the case of Ce$_{63}$O$_{216}$, the core of the cluster included: a Ce atom in the center (Ce$_1$) with the eight nearest oxygen neighbors (O$_1$) and 12 cerium sites of the next metal coordination sphere with their 48 nearest oxygen atoms. The other atoms of the cluster formed the "shell" and during self-consistency their electron densities and potentials were kept equivalent to those of Ce$_1$ and O$_1$. In the case of small fragment CeO$_8$, the renormalization procedure for the populations of oxygen atoms in valence atomic orbitals (AOs) during self-consistency was used in the calculations. The latter model of the boundary conditions for small clusters also allows one to include into the iterative scheme the stoichiometry of compounds and the possibility of charge redistribution between the outer atoms in the cluster and the surrounding crystal.

In this work, the calculations were carried out using the fully relativistic discrete-variational method (RDV)[25,26] with local exchange–correlation potential.[27] The RDV method is based on the solution of the Dirac–Slater equation for 4-component wave functions transforming according to the irreducible representations of the double point group (D_{4h} in the present calculations). For the calculation of symmetry coefficients we used the original code which realizes the projection operator technique[25] and includes the matrices of the irreducible representations of double point groups obtained in ref. 28 and the transformation matrices presented in ref. 29. The extended basis of 4-component numerical atomic orbitals (AOs) obtained as the solution of the Dirac–Slater equation for the isolated neutral atoms also included the vacant Ce 6p$_{1/2}$ and 6p$_{3/2}$ functions in addition to completely or partially occupied AOs. Numerical Diophantine integration in the calculations of matrix elements was carried out for 698 000 (Ce$_{63}$O$_{216}$) and 22 000 (CeO$_8$) sample points distributed in the cluster space. This provided the convergence of MO energies within 0.1 eV. The calculations of the electronic structure have been proved to be one of the most accurate tools for the determination of the electronic structures of solids.[30–32]

3 Results and discussion

The valence XPS structure of CeO$_2$ (0 to ~50 eV BE) appears due to OVMO and IVMO formation, as well as due to other processes (Fig. 1). In order to evaluate the contributions of the other processes, the core-level XPS structure was analyzed. For more details see ref. 11. The present work considers only some of the core-level XPS spectra.

3.1 Core-level XPS structure of CeO$_2$

As shown in ref. 11, the Ce 3p$_{1/2}$, 3d-, 4s-, 4p-, 4d-, 5s spectra in the BE range from ~35 to ~1250 eV exhibit a complex structure due to the many-body perturbation and complex final states. After Ce 3d electron photoemission the ground final state Ce 3d^{9}4f^0 and the two excited final states 3d^{9}4f^{1}OVMO^{-1} and 3d^{9}5p^{5}np^1 appear. The final state Ce 3d^{9}5p^{5}np^1 was

16168 | Phys. Chem. Chem. Phys., 2018, 20, 16167–16175

This journal is © the Owner Societies 2018
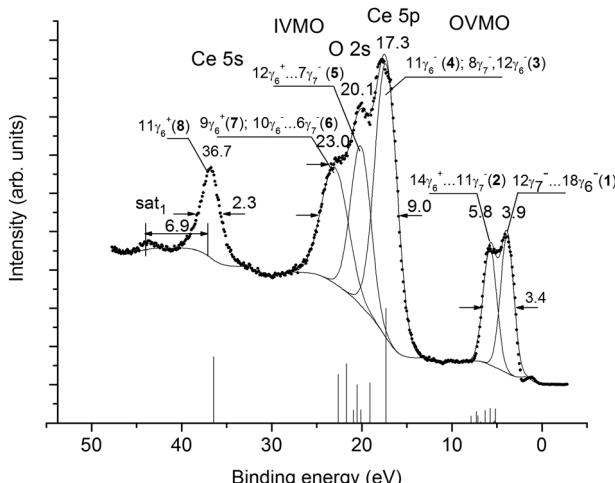
Fig. 1 Valence XPS spectrum of a single-crystalline (111) CeO$_2$ film on the Si(001) substrate. Vertical bars show the spectrum recorded for the CeO$_8$ cluster.

attributed to a weakly screened vacancy in the IVMO. As a result, the Ce 3d XPS spectrum exhibits a complicated structure instead of the expected doublet associated with the spin–orbit splitting ΔE_{sl}(Ce 3d) = 18.6 eV (Fig. 2). The same structures are observed in the XPS spectra of other core levels.[11] However, such a structure is not observed in the spectrum of Ce 5p electrons (Fig. 1). This confirms the appearance of the $3d^9 5p^5 np^1$ final state with a quasi-internal vacancy in the 5 p shell (Fig. 2).

Since the Ce^{4+} ions do not contain Ce 4f electrons, the corresponding spectra of the valence electrons do not show the structure associated with multiplet splitting (Fig. 1). As shown in ref. 21, the dynamic effect due to the giant Coster–Kronig transitions is expected in the Ce 4p XPS spectrum. The many-body perturbation[11,21] is one of the main reasons for the complex

structure in the core-level XPS spectra. This structure appears in the Ce 5s XPS spectrum, but not in the Ce 5p XPS spectrum. This yields a conclusion that the valence (0 to ~35 eV) XPS structure appears mostly due to the OVMO and IVMO electrons.

The O 1s spectrum appears as a single peak at E_b(O 1s) = 529.4 eV with FWHM Γ(O 1s) = 1.3 eV (Fig. 3). On a higher BE side from the primary peak a small shoulder at E_b(O 1s) = 531.7 eV can be attributed to hydroxyl groups. The intensity ratio for these peaks is 80% (CeO$_2$) and 20% (OH$^-$). The O 2p and O 2s features related to the OH$^-$ groups increase the error in the XPS intensity measurements (Fig. 1). The BE differences between the valence- and the core-level peaks, as well as the results of cluster calculations were used for the interpretation of valence XPS structures.

3.2 Electronic structure of the clusters in CeO$_2$

The ground state electronic configuration of a cerium atom is [Xe] $5s^2 5p^6 4f^2 5d^0 6s^2 6p^0$, where [Xe] is the xenon electronic configuration. The total densities of occupied states (DOS) obtained for the central Ce$_1$ and O$_1$ atoms in the two clusters are shown in Fig. 4. A comparison of the DOS in Fig. 4 shows that the set of discrete molecular levels in the small CeO$_8$ fragment (we have broadened each MO level with a Lorentzian function of a constant width for all MOs) transforms to energy bands of various widths in the large Ce$_{63}$O$_{216}$ cluster. Note that the positions of the centers of gravity of the main bands in both fragments are close to each other. Moreover, the analysis of covalent mixing of Ce 5p$_{1/2}$, 5p$_{3/2}$ with O 2s orbitals and Ce 4f$_{5/2}$, 4f$_{7/2}$, 5d$_{3/2}$, 5d$_{5/2}$, 6s, 6p$_{1/2}$ and 6p$_{3/2}$ with O 2p AOs shows that the main features of hybridization between metal and oxygen states are also similar in the two clusters. Note that the only visible difference between these spectra is the increase in energy difference between the highest occupied MO (HOMO) and the Ce 4s peak (−37.5 eV) in the large cluster by 0.5 eV. As seen in Fig. 1, this increase would improve the agreement with experiment. However, since in the large fragment, the energy region under investigation (−40 to 0 eV) contains 2231 orbitals,
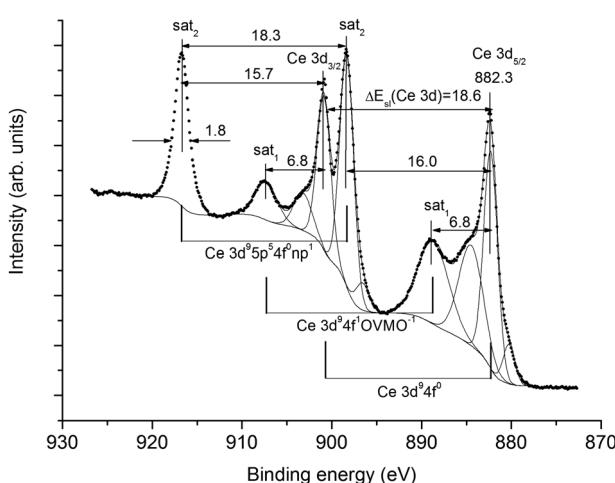
Fig. 2 Ce 3d XPS spectrum of a single-crystalline (111) CeO$_2$ film on the Si(001) substrate. Structures associated with the ground Ce $3d^9 4f^0$ and excited Ce $3d^9 4f^1$VMO^{-1} and Ce $3d^9 5p^5 4f^0 np^1$ final states are shown in the spectrum.
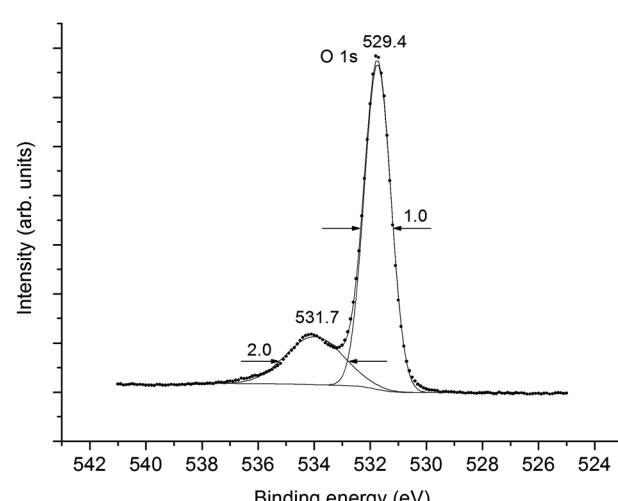
Fig. 3 An XPS narrow-scan of O 1s of the single-crystalline CeO$_2$ film.

This journal is © the Owner Societies 2018

Phys. Chem. Chem. Phys., 2018, 20, 16167–16175 | 16169
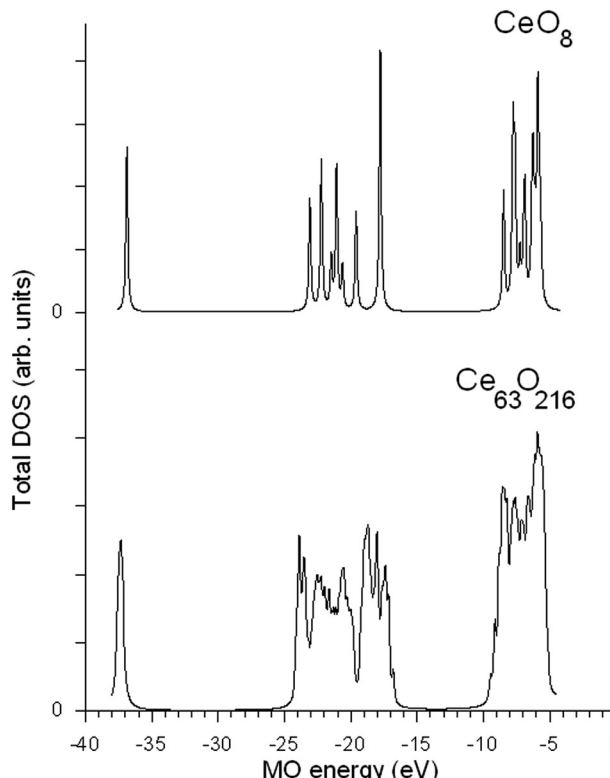
Fig. 4 Total DOS for the central part of CeO_8 and $Ce_{63}O_{216}$ clusters.

for the illustration of the general structure of the main molecular states, we use the results of RDV calculations for the small CeO_8 cluster. It is worth mentioning that in Fig. 1, the theoretical MO intensities were calculated using photoionization cross-sections.[33,34] The characteristics of all vacant and occupied MOs in the energy region from −40 to +15 eV obtained for this cluster are given in Table 1. The MO LCAO (Molecular Orbitals as Linear Combinations of Atomic Orbitals) approach was employed in order to consider the chemical bond in terms of atomic and molecular shells.

The IVMO and the OVMO formation is a result of the hybridization of Ce and O orbitals (Ce 5s, 5p, 4f, 6s and O 2s, 2p and empty Ce 5d, 6p AOs). Unlike the results of non-relativistic calculations for CeO_2 showing a significant participation of Ce 5s AO in MO formation,[18] the relativistic calculations show that Ce 5s states do not hybridize with oxygen orbitals (Table 1). The Ce 6s and 6p AOs take a notable part in the formation of vacant MOs. The Ce 4f AOs mostly participate in OVMO formation, while the Ce 5p, 5d AOs participate in both the OVMO and the IVMO. Especially a high mixing of the Ce $5p_{3/2}$ and the O 2s AOs was observed for the $12\gamma_6^-$, $8\gamma_7^-$ (3) and $10\gamma_6^-$, $6\gamma_7^-$ (6) IVMOs (Table 1). The hybridization of the Ce $5p_{1/2}$ and O 2s AOs in the $11\gamma_6^-$ (4) and $9\gamma_6^-$ (7) IVMOs is even higher due to a decrease in the BE difference between Ce $5p_{1/2}$ and O 2s levels (Fig. 1). These results together with the photoionization cross-sections[33,34] allow one to build a theoretical XPS spectrum (Table 2) and to interpret the corresponding experimental valence XPS spectral structure of CeO_2 (Fig. 1).

3.3 Valence XPS spectrum of CeO_2

The valence XPS spectrum exhibits several explicit features. This BE range can be subdivided into components (Fig. 1). Although formalistic, this subdivision allows one to compare the theoretical and experimental spectra of CeO_2 (Fig. 1 and Table 2).

The experimental spectrum reflects the excited electronic state with a hole in a level, while the theoretical spectrum corresponds to the ground state. Therefore, the BE values calculated for the transition state should be used.[35] However, it is known that the valence BEs calculated for the transition state usually differ from those for the ground state by a constant shift toward a higher value. Therefore, the BEs (Table 1) are increased by 5.14 eV (Table 2). With the MO composition (Table 1) and photoionization cross-sections in mind,[33,34] the intensities of the spectral ranges were calculated (Table 2). It has to be taken into account that CeO_2 XPS reflects the band structure and consists of bands widened due to the solid-state effects. Despite the approximation imperfection, a satisfactory quantitative agreement between the theoretical and experimental data was observed (Fig. 1 and Table 2).

The OVMO band can be subdivided into two components (1, 2) at 3.9 and 5.8 eV (Fig. 1 and Table 2). Component (1) is mostly due to the Ce 4f and O 2p electrons, while component (2) is due to the Ce 5d and O 2p electrons (Table 1). This agrees with the results of non-relativistic calculations for the CeO_8 cluster[18] and with the resonant emission (OVMO → Ce 4d[9]) spectroscopy data[36] for CeO_2. Under the resonant excitation at 124.8 eV, component (1) grows considerably at 3.56 eV. This confirms that this peak reflects the Ce 4f electronic states. The resonant emission spectrum of CeO_2 does not exhibit a feature at a lower energy side from the OVMO band associated with the Ce 4f electrons, whereas the corresponding spectrum of Ce_2O_3 exhibits this feature at 1.95 eV. This indicates that a stoichiometric CeO_2 consists of only Ce^{4+} ions. Thus, the Ce 4f related feature at 1.1 eV in the spectrum of CeO_2 (Fig. 1) appears due to Ce^{3+} ions formed on the surface under the Al K_α X-ray beam. In previous papers, the increase in the Ce^{3+} concentration on the surface of CeO_2 under the Al K_α X-ray beam[36,37] and increased temperature[5,38,39] were observed.

The IVMO spectrum can be formally subdivided into several ranges (Fig. 1 and Table 2). The Ce 5s spectrum does not show a 40% high-BE satellite with ΔE_{sat2} = 15 eV, the intensity of which was taken into account for the determination of the experimental intensity (15%) of the $11\gamma_6^+$ IVMO (Table 2). The calculated (Γ_T(OVMO) = 2.72 eV, I_T(OVMO) = 18% and I_T(IVMO) = 82%) and the experimental (Γ_E(OVMO) = 3.4 eV, I_E(OVMO) = 22% and I_E(IVMO) = 79%) data are comparable (Table 2 and Fig. 1). A satisfactory agreement between the theoretical and experimental BEs of some electronic shells was reached (Table 2). As noted, the non-relativistic calculations[18] allowed only a qualitative interpretation of the low-BE part of the valence XPS spectrum of CeO_2. The results of the present relativistic calculations allow a

16170 | Phys. Chem. Chem. Phys., 2018, 20, 16167–16175

This journal is © the Owner Societies 2018

Table 1 MO composition, energy $E_0{}^a$ (eV) and the photoionization cross-sections $\sigma_i{}^b$ for the CeO$_8$ cluster

MO	$-E_0$ (eV)	Ce 5s $\sigma_i{}^a$ 1.56	5p$_{1/2}$ 1.51	5p$_{3/2}$ 1.50	5d$_{3/2}$ 0.47	5d$_{5/2}$ 0.44	6s 0.15	4f$_{5/2}$ 0.97	4f$_{7/2}$ 0.93	6p$_{1/2}$ 0.89	6p$_{3/2}$ 0.86	O 2s 0.96	2p$_{1/2}$ 0.07	2p$_{3/2}$ 0.07
OVMO 19γ$_7{}^-$	−14.97			0.01							0.9	0.04	0.02	0.03
23γ$_6{}^-$	−14.95			0.01						0.01	0.9	0.04	0.01	0.03
22γ$_6{}^-$	−14.79		0.01							0.89	0.01	0.04	0.02	0.03
22γ$_6{}^+$	−12.63						0.88					0.05	0.02	0.05
19γ$_7{}^+$	−11.77					0.81						0.04	0.09	0.06
18γ$_7{}^+$	−11.59				0.45	0.36						0.04	0.04	0.11
21γ$_6{}^+$	−11.58				0.46	0.35						0.04	0.02	0.13
20γ$_6{}^+$	−7.5				0.38	0.50							0.04	0.08
17γ$_7{}^+$	−7.5				0.38	0.50							0.04	0.08
18γ$_7{}^-$	−4.17							0.18	0.69			0.01	0.05	0.07
21γ$_6{}^-$	−3.71							0.94	0.01				0.05	
17γ$_7{}^-$	−3.68							0.01	0.94				0.01	0.04
20γ$_6{}^-$	−3.68							0.01	0.94				0.01	0.04
16γ$_7{}^-$	−3.41							0.74	0.22				0.01	0.03
19γ$_6{}^-$	−3.35							0.92	0.02	0.01				0.05
15γ$_7{}^-$	−3.35							0.93	0.02					0.05
18γ$_6{}^{-\,c}$	0												0.31	0.69
14γ$_7{}^-$	0												0.31	0.69
13γ$_7{}^-$	0.13			0.04				0.04	0.02	0.01			0.21	0.68
17γ$_6{}^-$	0.13			0.04				0.04	0.01	0.01			0.13	0.77
19γ$_6{}^+$	0.22												0.16	0.84
16γ$_7{}^+$	0.22												0.15	0.85
18γ$_6{}^+$	0.23												0.66	0.34
16γ$_6{}^-$	0.58		0.02						0.05				0.72	0.21
15γ$_7{}^+$	0.58					0.01							0.06	0.93
14γ$_7{}^+$	0.6				0.01	0.01							0.48	0.50
17γ$_6{}^+$	0.6				0.01	0.01							0.46	0.52
12γ$_7{}^-$	0.66							0.06	0.07				0.29	0.58
11γ$_7{}^-$	1.14			0.01				0.01	0.01		0.04		0.25	0.68
15γ$_6{}^-$	1.14			0.01				0.01			0.04		0.13	0.81
14γ$_6{}^-$	1.27		0.01							0.05			0.44	0.50
16γ$_6{}^+$	1.65	0.01					0.06					0.01	0.31	0.61
10γ$_7{}^-$	1.94							0.01	0.02				0.17	0.80
13γ$_6{}^-$	1.94							0.01	0.02				0.17	0.80
9γ$_7{}^-$	1.94							0.02	0.02				0.64	0.32
13γ$_7{}^+$	2.12				0.05	0.08						0.01	0.08	0.78
15γ$_6{}^+$	2.12				0.08	0.05						0.01	0.03	0.83
12γ$_7{}^+$	2.13				0.03	0.10						0.01	0.76	0.10
11γ$_7{}^+$	2.71				0.05	0.07							0.29	0.59
14γ$_6{}^+$	2.72				0.05	0.07							0.30	0.58
IVMO 12γ$_6{}^-$	12.16			0.69							0.02	0.24	0.01	0.04
8γ$_7{}^-$	12.16			0.69							0.02	0.24	0.02	0.03
11γ$_6{}^-$	13.96		0.41							0.03		0.54	0.01	0.01
7γ$_7{}^-$	14.95							0.01	0.01			0.98		
10γ$_7{}^+$	15.37				0.01	0.03						0.96		
9γ$_7{}^+$	15.37				0.02	0.03						0.95		
13γ$_6{}^+$	15.37				0.03	0.02						0.95		
12γ$_6{}^+$	15.77	0.01					0.06					0.93		
6γ$_7{}^-$	16.55			0.25							0.02	0.71	0.01	0.01
10γ$_6{}^-$	16.55			0.25							0.02	0.72		0.01
9γ$_6{}^-$	17.45		0.55							0.01		0.42	0.01	0.01
11γ$_6{}^+$	31.31	0.98										0.01		0.01

^{a} Levels shifted by 13.01 eV toward the positive values (upward). ^{b} Photoionization cross-sections σ_i (kiloBarn per electron) from ref. 33. ^{c} Highest occupied MO (HOMO; 2 electrons), the occupation number for all the orbitals is 2.

satisfactory quantitative identification of the CeO$_2$ valence XPS spectrum in the BE range from 0 to ∼50 eV (Table 2 and Fig. 1). These data will promote the development of the RDV method and help to understand the chemical bond nature and to construct a quantitative MO scheme in CeO$_2$.

3.4 Molecular orbital scheme of CeO$_2$

With the BE differences between the valence- and the core-level peaks, as well as the calculation results for atomic[34] Ce and the CeO$_8$ cluster, a quantitative scheme of the molecular orbitals for CeO$_2$ was built (Fig. 5). In the accepted approximation one

Table 2 Parameters of CeO$_2$ XPS spectra, CeO$_8$ cluster and Ce 5p and Ce 4f DOS ρ_i (e$^-$)

MO		$-E^a$ (eV)	XPS Energy^b (eV) Experiment	Intensity, % Theory	Intensity, % Experiment	Ce 5p,4f DOS ρ_i e$^-$ (electron) 4f$_{5/2}$	4f$_{7/2}$	5p$_{1/2}$	5p$_{3/2}$
OVMO	18γ$_6^{-c}$	5.14	3.9 (1.7)	0.2	12				
	14γ$_7^-$	5.14		0.2					
	13γ$_7^-$	5.27		1.8		0.08	0.04		0.08
	17γ$_6^-$	5.27		1.7		0.08	0.02		0.08
	19γ$_6^+$	5.34		0.2					
	16γ$_7^+$	5.34		0.2					
	18γ$_6^+$	5.37		0.2					
	16γ$_6^-$	5.72		0.9			0.1	0.08	
	15γ$_7^+$	5.72		0.3					
	14γ$_7^+$	5.74		0.3					
	17γ$_6^+$	5.74		0.3					
	12γ$_7^-$	5.80	5.8 (1.8)	1.8	10	0.12	0.14		
	11γ$_7^-$	6.28		1.1		0.02	0.02		0.02
	15γ$_6^-$	6.28		1.0		0.02			0.02
	14γ$_6^-$	6.41		1.0				0.04	
	16γ$_6^+$	6.79		0.6					
	10γ$_7^-$	7.08		0.6		0.02	0.04		
	13γ$_6^-$	7.08		0.6		0.02	0.04		
	9γ$_7^-$	7.08		0.7		0.04	0.04		
	13γ$_7^+$	7.26		1.0					
	15γ$_6^+$	7.26		1.0					
	12γ$_7^+$	7.27		0.9					
	11γ$_7^+$	7.85		0.9					
	14γ$_6^+$	7.86		0.9					
	ΣI$_i^d$			18.4	22	0.4	0.44	0.12	0.2
IVMO	12γ$_6^-$	17.30	17.3 (2.9)	14.3	38				1.38
	8γ$_7^-$	17.30		14.3					1.38
	11γ$_6^-$	19.10		10.0				0.82	
	7γ$_7^-$	20.09	20.1 (2.6)	3.3	20	0.02	0.02		
	10γ$_7^+$	20.51		3.2					
	9γ$_7^+$	20.51		3.2					
	13γ$_6^+$	20.51		3.2					
	12γ$_6^+$	20.91		3.2					
	6γ$_7^-$	21.69	23.0 (3.5)	7.4	20				0.5
	10γ$_6^-$	21.69		7.4					0.5
	9γ$_6^-$	22.59		12.1				1.10	
	ΣI$_i^d$			81.6	79	0.02	0.02	1.92	3.76
	11γ$_6^+$	36.45	36.7 (2.4)	~16.5	15				

^{a} Energies shifted toward higher values (down) by 5.14 eV. ^{b} FWHMs are given in the parentheses in eV. ^{c} The highest occupied MO (2 electrons), the occupation number for other orbitals is 2. ^{d} Total intensities and Ce 5p, 4f DOS.

can formally separate the antibonding 12γ$_6^-$, 8γ$_7^-$ (3) and 11γ$_6^-$ (4) and the corresponding bonding 10γ$_6^-$, 6γ$_7$ (6) and 9γ$_6^-$ (7) IVMOs, as well as the quasiatomic 7γ$_7^-$, 10γ$_7^+$, 9γ$_7^+$, 13γ$_6^+$ and 12γ$_6^+$ (5) IVMOs associated mostly with the O 2s states which have to be close in magnitude.

Indeed, the O 1s spectrum of CeO$_2$ allows one to evaluate that the inequality of O 2s states must not exceed 1 eV, since the O 1s peak was observed to be sharp (Γ = 1.0 eV) and symmetric (Fig. 3). The O 2s BE must be E_b(O 2s) = 21.1 eV, since for atomic oxygen $\Delta E_O = E_b$(O 1s) − E_b(O 2s) = 508.3 eV[34] and the O 1s BE is E_b = 529.4 eV (Fig. 3). These data partially agree with the results of theoretical calculations (Table 2). Taking into account that the calculated BE difference for Ce atoms is ΔE_{Ce}^T = 864.5 eV (E_b(Ce 3d$_{5/2}$) = 883.3 eV and E_b(Ce 5p$_{3/2}$) = 18.8 eV),[34] while the difference between the Ce 3d$_{5/2}$ and 12γ$_6^-$, 8γ$_7^-$ (3) IVMO is ΔE_1 = 865.0 eV, one can find that Δ_1 = 0.5 eV (Fig. 5).

This confirms the antibonding nature of the 12γ$_6^-$, 8γ$_7^-$ (3) IVMO. The FWHM of the IVMO XPS features does not allow to arrive at a conclusion on their bonding or antibonding nature. However, one can suggest that these orbitals partially lose their antibonding nature (Table 2 and Fig. 5, see also ref. 40) due to the contribution of 5% of the O 2p and 2% of the Ce 6p AO in the 12γ$_6^-$, 8γ$_7^-$ (3) IVMO.

3.5 Contribution of valence electrons to the chemical bond in CeO$_2$

In this work, we used the values of overlap populations (n_{ij}) of various pairs of metal and oxygen AOs[41] to evaluate their contributions to the chemical bond. Table 3 shows these values for the outer and inner valence electrons obtained in the non-relativistic (NDV) and relativistic (RDV) calculations. Positive and negative values correspond to the bonding and

16172 | *Phys. Chem. Chem. Phys.*, 2018, **20**, 16167–16175

This journal is © the Owner Societies 2018
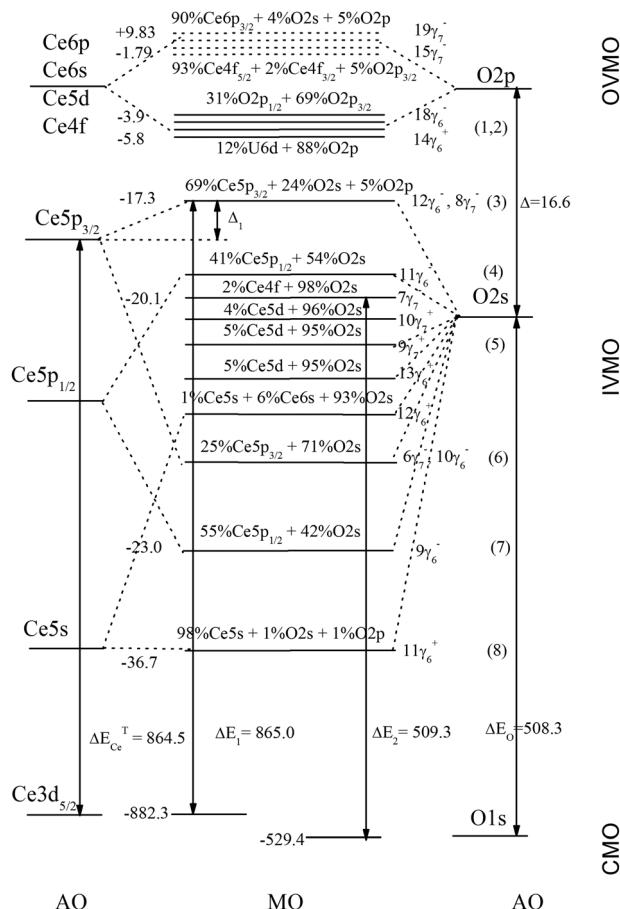
Fig. 5 Molecular orbital scheme for the CeO$_8$ cluster built on the basis of theoretical and experimental data. Chemical shift is not shown. Arrows indicate experimentally measured BE differences. Experimental BEs (eV) are shown on the left. The energy scale is not shown.

Table 3 Overlap populations for CeO$_2$ (per one ligand, $\times 10^3$), obtained in the relativistic (RDV) and non-relativistic (NDV) calculations of the CeO$_8$ cluster

Bonds in CeO$_2$	RDV[a]			NDV
	Partial	Total		
Ce 4f$_{5/2}$–O 2p$_{1/2}$; O 2p$_{3/2}$	1; 21	49		43
Ce 4f$_{7/2}$–O 2p$_{1/2}$; O 2p$_{3/2}$	15; 12			
Ce 4f$_{5/2}$–O 2s	3			
Ce 4f$_{7/2}$–O 2s	4	7		5
Ce 6p$_{1/2}$–O 2p$_{1/2}$; O 2p$_{3/2}$	18; 5			
Ce 6p$_{3/2}$–O 2p$_{1/2}$; O 2p$_{3/2}$	3; 42	68		67
Ce 6p$_{1/2}$–O 2s	11			
Ce 6p$_{3/2}$–O 2s	19	30		27
Ce 6s–O 2p$_{1/2}$; O 2p$_{3/2}$	4; 7	11		5
Ce 6s–O 2s	26	26		27
Ce 5d$_{3/2}$–O 2p$_{1/2}$; O 2p$_{3/2}$	4; 72			
Ce 5d$_{5/2}$–O 2p$_{1/2}$; O 2p$_{3/2}$	58; 55	189		179
Ce 5d$_{3/2}$–O 2s	12			
Ce 5d$_{5/2}$–O 2s	19	31		30
Σ_{OVMO}[b]	411	411		383
Ce 5p$_{1/2}$–O 2p$_{1/2}$; O 2p$_{3/2}$	−8; −18			
Ce 5p$_{3/2}$–O 2p$_{1/2}$; O 2p$_{3/2}$	−23; −40	−89		−91
Ce 5p$_{1/2}$–O 2s	−7			
Ce 5p$_{3/2}$–O 2s	−21	−28		−31
Ce 5s–O 2p$_{1/2}$; O 2p$_{3/2}$	−10; −20	−30		−37
Ce 5s–O 2s	−3	−3		−5
Σ_{IVMO}[b]	−150	−150		−164

[a] Partial and total contribution. [b] Total OVMO and IVMO contribution.

antibonding interactions, respectively. The relativistic and non-relativistic results differ slightly. For example, the contribution from the Ce 4f–O 2p, Ce 6s–O 2p and Ce 5d–O 2p bonds increases in the relativistic approach, which reveals the bonding nature of these states. The Ce 5s–O 2s, 2p interactions are less antibonding in the non-relativistic calculation than in the relativistic one. This can be explained by the fact that in the relativistic calculation, the Ce 5s BE increases significantly compared to that calculated in the non-relativistic approach.

The contribution to bonding from the outer valence shells in CeO$_2$ is (411) (Table 3). The largest bonding contributions come from the Ce 4f–O 2p (49), Ce 6p–O 2p (68) and Ce 5d–O 2p (189) AOs. The inner valence electrons of Ce provide the total antibonding contribution of −150. The highest antibonding contribution is obtained from the Ce 5p–O 2p (−89) states. To summarize, the IVMO electrons weaken the chemical bond by 37%. The total contribution of the valence electrons to the chemical bond in CeO$_2$ is 261.

4 Conclusions

On the basis of the relativistic cluster calculations, a quantitative interpretation of the outer (0 to ∼15 eV BE) and inner (∼15 to ∼50 eV BE) valence XPS spectral structures of CeO$_2$ was performed.

It was theoretically shown and experimentally confirmed that the Ce 4f electrons (0.86 of the Ce 4f electron) participate directly in chemical bond formation in CeO$_2$ partially losing the f-character. The contributions from Ce 4f orbitals are located mainly within the outer valence band.

It was found that the Ce 5p electrons not only participate effectively (experimentally measurable) in the formation of the IVMO, but also participate noticeably in the formation of the occupied OVMO (0.32 of the Ce 5p electron). The largest part in the IVMO formation is taken by the Ce 5p$_{1/2}$, 5p$_{3/2}$ and the O 2s AOs of the neighboring cerium and oxygen. The Ce 5s electrons participate weakly in the chemical bond formation.

The composition and the sequent order of the molecular orbitals in the binding energy range from 0 to ∼50 eV were established. A quantitative scheme of the molecular orbitals for CeO$_2$ was built. This scheme is fundamental for understanding the nature of chemical bonding and for the interpretation of other X-ray spectra of CeO$_2$. The evaluation of the contribution from various electrons to the chemical bond revealed that the antibonding contribution from IVMO electrons is near 37% of the chemical bond formed by the OVMO electrons.

Conflicts of interest

There are no conflicts to declare.

Acknowledgements

References

1 P. D. Edmondson, Y. Zhang, S. Moll, F. Namavar and W. J. Weber, Irradiation effects on microstructure change in nanocrystalline ceria – Phase, lattice stress, grain size and boundaries, *Acta Mater.*, 2012, **60**, 5408–5416.

2 M. Kinoshita, K. Yasunaga, T. Sonoda, A. Iwase, N. Ishikawa, M. Sataka, K. Yasuda, S. Matsumura, H. Y. Geng, T. Ichinomiya, Y. Chen, Y. Kaneta, M. Iwasawa, T. Ohnuma, Y. Nishiura, J. Nakamura and H. Matzke, Recovery and restructuring induced by fission energy ions in high burnup nuclear fuel, *Nucl. Instrum. Methods Phys. Res., Sect. B*, 2009, **267**, 960–963.

3 B. E. Burakov, M. I. Ojovan and W. E. Lee, Crystalline Materials for Actinide Immobilisation, in *Materials for Engineering*, ed. W. E. Lee, Imperial College Press, London, 2011, vol. 1, pp. 58–59.

4 D. R. Mullins, S. H. Overbury and D. R. Huntley, Electron spectroscopy of single crystal and polycrystalline cerium oxide surfaces, *Surf. Sci.*, 1998, **409**, 307–319.

5 V. Stetsovych, F. Pagliuca, F. Dvorak, T. Duchon, M. Vorokhta, M. Aulicka, J. Lachnitt, S. Schernich, I. Matolinova, K. Veltruska, T. Skala, D. Mazur, J. Myslivecek, J. Libuda and V. Matolin, Epitaxial Cubic Ce_2O_3 Films via Ce-CeO_2 Interfacial Reaction, *J. Phys. Chem. Lett.*, 2013, **4**, 866–871.

6 Y. Zhu, N. Jain, M. K. Hudait, D. Maurya, R. Varghese and S. Priya, X-ray photoelectron spectroscopy analysis and band offset determination of CeO_2 deposited on epitaxial (100), (110), and (111)Ge, *J. Vac. Sci. Technol., B*, 2014, **32**, 011217.

7 P. Burroughs, A. Hamnett, A. F. Orchard and G. Thornton, Satellite structure in the X-ray photoelectron spectra of some binary and mixed oxides of lanthanum and cerium, *J. Chem. Soc., Dalton Trans.*, 1976, 1686–1698.

8 Yu. A. Teterin and A. S. Baev, *Rentgenovskaya Fotoelektronnaya Spektroskopiya Soedinenii Lantanoidov (X-ray Photoelectron Spectroscopy of Lanthanide Compounds)*, TsNII atominform, Moscow, 1987 (in Russian).

9 Yu. A. Teterin and A. Yu. Teterin, Structure of X-ray photoelectron spectra of lanthanide compound, *Russ. Chem. Rev.*, 2002, **71**, 347–381.

10 Yu. A. Teterin, S. V. Stefanovskiĭ, S. V. Yudintsev, G. N. Bek-Uzarov, A. Yu. Teterin, K. I. Maslakov and I. O. Utkin, X-ray photoelectron study of calcium cerium titanate ceramics, *Russ. J. Inorg. Chem.*, 2004, **49**, 87–94.

11 K. I. Maslakov, Yu. A. Teterin, A. J. Popel, A. Yu. Teterin, K. E. Ivanov, S. N. Kalmykov, V. G. Petrov, P. K. Petrov and I. Farnan, XPS study of ion irradiated and unirradiated CeO_2 bulk and thin film samples, *Appl. Surf. Sci.*, 2018, **448**, 154–162.

12 A. Kotani, T. Jo and J. C. Parlebas, Many-body effects in core-level spectroscopy of rare-earth compounds, *Adv. Phys.*, 1988, **37**, 37–85.

13 A. Kotani and H. Ogasawara, Theory of core-level spectroscopy of rare-earth oxides, *J. Electron Spectrosc. Relat. Phenom.*, 1992, **60**, 257–299.

14 A. Fujimori, Mixed-valent ground state of CeO_2, *Phys. Rev. B: Condens. Matter Mater. Phys.*, 1983, **28**, 2281–2283.

15 A. Kotani, Theory of core-level spectroscopy in f and d electron systems, *J. Electron Spectrosc. Relat. Phenom.*, 1999, **100**, 75–104.

16 E. Shoko, M. F. Smith and R. H. McKenzie, Mixed valency in cerium oxide crystallographic phases: Valence of different cerium sites by the bond valence method, *Phys. Rev. B: Condens. Matter Mater. Phys.*, 2009, **79**, 134108.

17 G. Thornton and M. J. Dempsey, Final-state effects in the 3d and 4d X-ray photoelectron spectra of CeO_2, *Chem. Phys. Lett.*, 1981, **77**, 409–412.

18 M. V. Ryzhkov, V. A. Gubanov, Yu. A. Teterin and A. S. Baev, Electronic structure, chemical bonding and X-ray photo-electron spectra of light rare-earth oxides, *Z. Phys. B: Condens. Matter*, 1985, **59**, 1–6.

19 Yu. A. Teterin, A. Yu. Teterin, A. M. Lebedev and I. O. Utkin, The XPS spectra of cerium compounds containing oxygen, *J. Electron Spectrosc. Relat. Phenom.*, 1998, **88–91**, 275–279.

20 A. J. Popel, S. Le Solliec, G. I. Lampronti, J. Day, P. K. Petrov and I. Farnan, The effect of fission-energy Xe ion irradiation on the structural integrity and dissolution of the CeO_2 matrix, *J. Nucl. Mater.*, 2017, **484**, 332–338.

21 Yu. A. Teterin and A. Yu, Teterin, The structure of X-ray photoelectron spectra of light actinide compounds, *Russ. Chem. Rev.*, 2004, **73**, 541–580.

22 D. Shirley, High-Resolution X-ray Photoemission Spectrum of the Valence Bands of Gold, *Phys. Rev. B: Solid State*, 1972, **5**, 4709–4714.

23 M. Wolcyrz and L. Kepinski, Rietveld refinement of the structure of CeOCl formed in Pd/CeO_2 catalyst: Notes on the existence of a stabilized tetragonal phase of La_2O_3 in LaPdO system, *J. Solid State Chem.*, 1992, **99**, 409–413.

24 M. V. Ryzhkov, N. I. Medvedeva and V. A. Gubanov, Sub-stitution of Pb by Ag as a way to obtain new high tempera-ture superconductors: A quantum chemical point of view, *J. Phys. Chem. Solids*, 1995, **56**, 1231–1237.

25 A. Rosen and D. E. Ellis, Relativistic molecular calculations in the Dirac–Slater model, *J. Chem. Phys.*, 1975, **62**, 3039–3049.

26 D. E. Ellis and G. L. Goodman, Self-consistent Dirac–Slater calculations for molecules and embedded clusters, *Int. J. Quantum Chem.*, 1984, **25**, 185–200.

27 O. Gunnarsson and B. I. Lundqvist, Exchange and correlation in atoms, molecules, and solids by the spin-density-functional formalism, *Phys. Rev. B: Solid State*, 1976, **13**, 4274–4298.

16174 | *Phys. Chem. Chem. Phys.*, 2018, **20**, 16167–16175

This journal is © the Owner Societies 2018

28 P. Pyykkö and H. Toivonen, Tables of Representation and Rotation Matrices for the Relativistic Irreducible Representations of 38 Point Groups, *Acta Acad. Abo., Ser. B*, 1983, **43**, 1–50.

29 D. A. Varshalovich, A. N. Moskalev and V. K. Khersonskii, *Quantum Theory of Angular Momentum*, World Scientific, 1988.

30 A. H. Reshak, Thermoelectric properties for AA- and AB-stacking of a carbon nitride polymorph (C_3N_4), *RSC Adv.*, 2014, **4**, 63137–63142.

31 G. E. Davydyuk, O. Y. Khyzhun, A. H. Reshak, H. Kamarudin, G. L. Myronchuk, S. P. Danylchuk, A. O. Fedorchuk, L. V. Piskach, M. Y. Mozolyuk and O. V. Parasyuk, Photoelectrical properties and the electronic structure of $Tl_{1-x}In_{1-x}Sn_xSe_2$ (x = 0, 0.1, 0.2, 0.25) single crystalline alloys, *Phys. Chem. Chem. Phys.*, 2013, **15**, 6965–6972.

32 A. H. Reshak, Ab initio study of TaON, an active photocatalyst under visible light irradiation, *Phys. Chem. Chem. Phys.*, 2014, **16**, 10558–10565.

33 I. M. Band, Y. I. Kharitonov and M. B. Trzhaskovskaya, Photoionization cross sections and photoelectron angular distributions for X-ray line energies in the range 0.132–4.509 keV targets: $1 \leq Z \leq 100$, *At. Data Nucl. Data Tables*, 1979, **23**, 443–505.

34 M. B. Trzhaskovskaya and V. G. Yarzhemsky, Dirac–Fock photoionization parameters for HAXPES applications, *At. Data Nucl. Data Tables*, 2018, **119**, 99–174.

35 J. C. Slater and K. H. Johnson, Self-Consistent-Field Xα Cluster Method for Polyatomic Molecules and Solids, *Phys. Rev. B: Solid State*, 1972, **5**, 844–853.

36 M. V. Rama Rao and T. Shripathi, Photoelectron spectroscopic study of X-ray induced reduction of CeO_2, *J. Electron Spectrosc. Relat. Phenom.*, 1997, **87**, 121–126.

37 E. Paparazzo, G. M. Ingo and N. Zacchetti, X-ray induced reduction effects at CeO_2 surfaces: An X-ray photoelectron spectroscopy study, *J. Vac. Sci. Technol., A*, 1991, **9**, 1416–1420.

38 F. Le Normand, J. El Fallah, L. Hilaire, P. Légaré, A. Kotani and J. C. Parlebas, Photoemission on 3d core levels of Cerium: An experimental and theoretical investigation of the reduction of cerium dioxide, *Solid State Commun.*, 1989, **71**, 885–889.

39 T. Hasegawa, S. M. Shahed, Y. Sainoo, A. Beniya, N. Isomura, Y. Watanabe and T. Komeda, Epitaxial growth of CeO_2(111) film on Ru(0001): scanning tunneling microscopy (STM) and X-ray photoemission spectroscopy (XPS) study, *J. Chem. Phys.*, 2014, **140**, 044711.

40 Yu. A. Teterin and S. G. Gagarin, Inner valence molecular orbitals and the structure of X-ray photoelectron spectra, *Russ. Chem. Rev.*, 1996, **65**, 825–847.

41 R. S. Mulliken, Chemical Bonding, *Annu. Rev. Phys. Chem.*, 1978, **29**, 1–31.